Robust ferromagnetism in the compressed permanent magnet Sm$_2$Co$_{17}$

J. R. Jeffries,[1] L. S. I. Veiga,[2,3,4] G. Fabbris,[2,5] D. Haskel,[2] P. Huang,[1,6] N. P. Butch,[7] S. K. McCall,[1]
K. Holliday,[1] Z. Jenei,[1] Y. Xiao,[8] and P. Chow[8]

[1]*Condensed Matter and Materials Division, Lawrence Livermore National Laboratory, Livermore, California 94550, USA*
[2]*Advanced Photon Source, Argonne National Laboratory, Argonne, Illinois 60439, USA*
[3]*Instituto de Física "Gleb Wataghin", Universidade Estadual de Campinas, Campinas, São Paulo 13083-859, Brazil*
[4]*Laboratório Nacional de Luz Síncrotron, Campinas, São Paulo 13083-970, Brazil*
[5]*Department of Physics, Washington University, St. Louis, Missouri 63130 USA*
[6]*Department of Chemistry and Biochemistry, California State University, East Bay, Hayward, California 94542, USA*
[7]*NIST Center for Neutron Research, National Institute of Standards and Technology, Gaithersburg, Maryland 20899, USA*
[8]*HP-CAT, Geophysical Laboratory, Carnegie Institute of Washington, Argonne, Illinois 60439, USA*

The compound Sm$_2$Co$_{17}$ displays magnetic properties amenable to permanent magnet applications owing to both the $3d$ electrons of Co and the $4f$ electrons of Sm. The long-standing description of the magnetic interactions between the Sm and Co ions implies a truly ferromagnetic configuration, but some recent calculations challenge this axiom, suggesting at least a propensity for ferrimagnetic behavior. We have used high-pressure synchrotron x-ray techniques to characterize the magnetic and structural properties of Sm$_2$Co$_{17}$ to reveal a robust ferromagnetic state. The local Sm moment is at most weakly affected by compression, and the ordered moments show a surprising resilience to volumetric compressions of nearly 20%. Density functional theory calculations echo the magnetic robustness of Sm$_2$Co$_{17}$.

I. INTRODUCTION

Permanent magnets have found applications since antiquity, but the purview of their technological impact has exploded in the recent decades, serving as key components in motors, actuators, and sensors. Their application space has greatly expanded due to the development of high-strength permanent magnets based on intermetallic compounds composed of rare-earth (RE) and transition-metal (TM) elements. These magnets have been built on a century of materials research and optimization beginning with steels and culminating in the development of the most commonly deployed Nd$_2$Fe$_{14}$B permanent magnets [1,2].

Along with the Curie temperature T_C, the principal figure of merit for a permanent magnet is the energy density $|BH_{max}|$ (measured in the second quadrant of a hysteresis loop), which is effectively controlled by two properties: the remanence and the coercivity [3]. Materials with high remanence, the magnetization remaining in zero external field, have always relied upon the unpaired electrons of the $3d$ transition metals (e.g., Mn, Fe, Co, Ni), but the coercivity, the material's resistance to demagnetization, derives from different mechanisms: shape anisotropy arising from microstructural morphology; defects and impurities which act as pinning centers for magnetic domain walls; and, at a fundamental level, the magnetocrystalline anisotropy (MCA). In the 20th century, the first truly hard magnets developed were the alnico magnets, which exploit shape anisotropy by burying oriented nanoscale CoFe needles within an AlNi matrix [4]. Modern RE-based magnets take advantage of the inherent (MCA) generated by the interaction of the $4f$-electron orbitals with the large crystalline electric field (CEF) arising from the anisotropic crystalline environment. When the easy axis of magnetization lies along a low-symmetry crystallographic direction, very large coercivities are often observed, and this

coercivity combined with the substantial magnetic moment of the TM atoms makes these intermetallic compounds choice materials for permanent magnet applications. The exceptional performance of the Nd$_2$Fe$_{14}$B permanent magnet sets a high bar for new materials, and little progress has been made in the last few decades with respect to identifying a competitive variant. However, with increasing demand for high-performance magnets, and the uncertainty in the supply of RE elements, there is a growing interest in permanent magnets with reduced RE element content.

Although the Sm-Co systems were introduced and studied in the 1970s and 1980s [5], renewed interest in permanent magnets has rekindled the study of these materials. Many researchers have focused on the Sm-Co family of permanent magnets because their Curie temperatures ($T_C \sim 1000$ K) are much higher than that of Nd$_2$Fe$_{14}$B ($T_C = 588$ K), making the former attractive in motor or generator applications where high temperatures could degrade the performance of Nd$_2$Fe$_{14}$B systems. Researchers have embarked on many routes to improve the performance of Sm-Co magnetic materials including substitution [6,7], thin-film synthesis [8], composites [9], and microstructure modifications [10–12]. Like Nd$_2$Fe$_{14}$B, Sm$_2$Co$_{17}$ forms in an anisotropic crystal structure composed of TM and TM-RE atomic planes stacked along a c axis. Sm$_2$Co$_{17}$ crystallizes in the $R\bar{3}m$ space group (Th$_2$Zn$_{17}$ type) with lattice constants $a = 8.4$ and $c = 12.2$ Å (hexagonal axes) and three formula units per unit cell [13]. The Sm$_2$Co$_{17}$ structure is effectively a modification of the SmCo$_5$ structure, which is composed of alternating planes of Co (only) and Sm-Co, with the Sm ions surrounded by a hexagonal net of Co atoms. The Sm$_2$Co$_{17}$ structure is formed by substituting $\frac{1}{3}$ of the Sm ions with a Co-Co dimer; the Co-Co spacing of the dimer is approximately 3% smaller than the spacing of the Co hexagonal net that surrounds it.

The 1-5 and 2-17 structures naturally provide the propensity for anisotropic CEF and substantial MCA; in fact, the Co atoms in YCo_5, $LaCo_5$, and $CeCo_5$ possess sizable MCA even though the RE ions in these compounds are nonmagnetic [14]. In Sm_2Co_{17}, the Co sublattice provides more than one third of the total MCA of the system [15]. In addition to the Co sublattice of Sm_2Co_{17}, the Sm ions contribute substantially to the magnetic properties. The single-ion CEF interaction of the Sm ions is uniaxial and thus orients the Sm moments along the c axis of the crystal structure [3]. Early in the study of the Sm-Co intermetallics, a Ruderman-Kittel-Kasuya-Yosida (RKKY) interaction was proposed as a mechanism coupling the Sm and Co atoms [5]. However, this RKKY interaction does not generically describe the behavior of both the light and heavy lanthanide systems. Instead, the picture that emerged to describe the $RECo_5$ and RE_2Co_{17} compounds was one where the Sm $4f$ electrons polarize (in a parallel orientation) the Sm $5d$ electrons via an onsite exchange interaction, and preferential hybridization between the spin-down Sm $5d$ and the Co $3d$ electrons yields an antiparallel spin configuration between the Sm and Co ions [16,17]. Because the orbital moment of Sm is expected to be larger than and opposite to its spin moment, the antiparallel Sm-Co spin coupling results in a parallel (ferromagnetic) configuration for the total Sm and Co moments. Some recent calculations challenge this picture, however, implying an opposite-polarization Sm $4f$-$5d$ exchange [18] or parallel Sm-Co spin alignments [19]. These new models suggest that the magnetic configuration of the Sm-Co system may not be as robust as once considered, and that ferrimagnetic configurations may be energetically competitive.

Pressure provides a thermodynamic parameter that can control structural parameters thereby altering CEF interactions and magnetic response. The results of high-pressure experiments are readily comparable with the outputs of modern computational methods, providing important benchmarks for understanding microscopic mechanisms of magnetism and evaluating the magnetic configuration across a broad swath of phase space. In this paper, we report a combined experimental and theoretical study of the permanent magnet Sm_2Co_{17} under compression. The experiments reveal an extremely robust ferromagnetic state under pressures up to approximately 40 GPa, and theory confirms this robustness, implying substantial moments on the Sm and Co ions up to at least 54 GPa.

II. EXPERIMENTAL AND THEORETICAL METHODS

A. Sample synthesis

Polycrystalline samples of Sm_2Co_{17} were synthesized with an arc-melting technique, and acquired from Sophisticated Alloys. The samples were annealed in Ar for three weeks at $800\,^{\circ}C$, and the crystal structure was confirmed with x-ray diffraction. X-ray photoemission spectroscopy confirmed the stoichiometry of the samples. Ambient-pressure magnetic characterization using a Quantum Design Magnetic Properties Measurement System revealed a saturation magnetization of 25.0 μ_B/f.u. and a coercivity ranging from less than 20 Oe for a 24.5-mg polycrystalline sample (approximately

a right cylinder) to almost 2 kOe for an aligned powder embedded in epoxy (Fig. 7).

B. High-pressure techniques

Pressure-dependent, angle-dispersive x-ray diffraction measurements were performed at beamline 16-BM-D at the Advanced Photon Source (APS) at Argonne National Laboratory. High pressures were generated with a gas-membrane-driven diamond anvil cell (DAC). The DAC was composed of two gem-quality diamond anvils with 300-μm culets. A rhenium gasket was preindented to a thickness of 40 μm, and a 130-μm diameter hole was drilled for the sample chamber. The powdered sample was loaded into the sample chamber along with copper powder, which served as the pressure marker. The sample chamber was loaded with Ne gas as the pressure-transmitting medium. The incident x-ray beam was focused to a 12×5 μm spot size with an incident energy of 30 keV ($\lambda = 0.4135$ Å). X-ray diffraction patterns were acquired with a Mar345 image plate using 120-s exposures. The two-dimensional (2D) diffraction patterns were integrated with the program FIT2D [20] to obtain conventional intensity versus 2Θ diffraction patterns. The lattice parameters were refined using the JADE software package.

High-pressure x-ray emission spectroscopy (XES) measurements were performed at sector 16-ID-D of the APS, using an identical gas-membrane-driven DAC. For these XES measurements, a beryllium gasket was indented and drilled with identical parameters to the XRD measurements described above. The sample was loaded in a Ne pressure-transmitting medium, and the pressure was determined using the shift of the ruby fluorescence line. The 11.3-keV, incident x-ray beam was focused to a 25×50 μm spot size. The incident beam entered through one of the anvils, and the Sm $L\gamma_1$ emission spectra were collected through the Be gasket using a bent Si (440) analyzer. At each pressure, 8–10 spectra were collected, normalized to the incident beam intensity, and summed to generate a final x-ray emission spectrum.

X-ray absorption near edge structure (XANES) and x-ray magnetic circular dichroism (XMCD) measurements were performed at the Co K edge and Sm L_3 edge at the 4-ID-D beamline of the APS. A nonmagnetic beryllium-copper DAC was used. Since measurements were performed in a transmission geometry through the diamond anvils, a set of mini-anvil plus fully perforated anvil was paired with a partially perforated anvil (300-μm culet diameter) in order to reduce attenuation of x-ray intensity and improve counting statistics. A rhenium gasket was preindented to a thickness of 40 μm and a 120-μm hole drilled for the sample chamber. The sample was powdered and mixed with mineral oil in a 2:1 ratio (by mass) to provide an optimal effective thickness for the absorption measurements. Pressure was calibrated using the ruby fluorescence method. A Pd toroidal mirror focused the x-ray beam, which was ultimately defined by 50×50 μm slits. Harmonic rejection was achieved by the combined use of a Si mirror and detuning of the second monochromator crystal. Incident and transmitted x-ray intensities were measured with Si photodiodes. A diamond phase retarder (180-μm thick) fitted with a PZT stage was used to generate circularly polarized x rays with alternating helicity (13.1 Hz) and XMCD

was measured by detecting the modulation in absorption coefficient at this frequency. The applied field was 3.5 T and any artifact in XMCD signals was removed by measuring XMCD with field parallel and antiparallel to the incident x-ray wave vector. The XANES/XMCD measurements were performed at 200 K.

C. Density functional theory calculations

First-principles calculations were performed using spin-polarized density functional theory (DFT) within the generalized gradient approximation (GGA) for the exchange-correlation energy functional. Specifically, we employ the GGA of Perdew, Burke, and Ernzerhof (PBE) [21]. The electronic wave functions were expanded in plane-wave basis sets truncated at a cutoff energy of 60 Ry; similarly, basis sets for the charge densities were truncated at 480 Ry. Brillouin zone integrations were performed on a $5 \times 5 \times 3$ k-point grid, and the Methfessel-Paxton broadening [22] was applied with a smearing width of 0.01 Ry. All plane-wave DFT calculations in this work were carried out using the QUANTUM ESPRESSO package [23].

The interaction between valence electrons and ionic cores were represented using Vanderbilt-type ultrasoft pseudopotentials (USP) [24]. The cobalt USP was constructed using parameters suggested by Moroni *et al.* [25] and treats nine electrons as valence. For samarium, the reference state for the pseudopotential generation was chosen to be a scalar relativistic description for the Sm^{3+} ion in the [Xe] $4f5$ configuration. Our Sm USP includes the $4f$ electrons as valence for a total of 16 valence electrons, as we found that explicit treatment of the Sm $4f$ was necessary for accurate equilibrium volumes. Pseudovalence wave functions were constructed using the pseudization procedure described by Rappe *et al.* [26] with cutoff distances of 1.7 a_0 for the s and p functions, and 2.0 a_0 for the d and f functions. Each angular momentum projector l is comprised of two states spanning an energy range of about 0.1 to 1 Ry. The local potential was taken to equal the all-electron potential beyond a cutoff distance of 1.7 a_0. A nonlinear core correction term [27] was also included which was pseudized using two Bessel functions within a cutoff distance of 1.2 a_0. The atomic module in the QUANTUM ESPRESSO package [23] was used for the pseudopotential generation.

Local and semilocal approximations for the exchange-correlation energy functional such as the GGA can exhibit large self-interaction errors when localized, open-shell electrons are involved, i.e., the Sm $4f$ electrons. Thus, we adopted a DFT+U approach that incorporates an additional Hubbard-type term to account for the strong, onsite Coulomb correlation effects between the Sm $4f$ electrons. Specifically, the rotationally invariant formulation of DFT+U due to Cococcioni and de Gironcoli [28] was employed. In short, the meaning of the "+U" term in this model can be interpreted as a penalty functional whose strength is tuned by a single parameter U, and favors the integer occupation of the localized states upon which it is applied. Following the procedure based on the linear-response theory proposed of Cococcioni and de Gironcoli [28], we derived a value of $U = 6.1$ eV for Sm_2Co_{17}. We emphasize that this value of U was not obtained by fitting

to experimental data, but was instead computed from first principles.

For the lanthanide elements, spin-orbit coupling involving the $4f$ shell contributes significantly to magnetic properties such as the total magnetic moment and the magnetocrystalline anisotropy. But, as the primary goal of our calculations was geometry optimization, spin-orbit effects were neglected here. The self-consistent inclusion of spin-orbit coupling in structure determination is a challenging task, and at present this is only tractable for relatively small systems. Calculations for small actinide molecules have found that spin-orbit effects modify bond lengths by <0.1 Å and vibrational frequencies by a few percent [29–31]; similarly, spin-orbit effects have little influence on lattice structures for the actinide dioxides [32]. Given the more compact nature of the lanthanide $4f$ wave functions as compared to the actinide $5f$ electrons, spin-orbit coupling is expected to play an even lesser role in bonding and thus the influence on geometry should be minimal.

III. RESULTS AND DISCUSSION

A. Equation of state

As an initial validation of our model, we compute the evolution of the crystal structure of Sm_2Co_{17} with pressure and compare with experiments. Figure 1 shows the calculated (open symbols) and measured (closed symbols) crystal structure parameters: the basal plane lattice parameter a, the c-axis lattice parameter, the c/a ratio, and the unit-cell volume. The ambient-pressure equilibrium unit-cell volume is calculated to be 758 Å^3, which slightly overestimates the experimental value of 753 Å^3; a 1% overestimation in the equilibrium volume of solids is typical behavior for the GGA approach. The calculated a- and c-axis lattice parameters are also very close to experiment. Furthermore, as shown in Fig. 1, the agreement between theory and experiment is maintained even with the application of pressure.

No structural phase transitions are seen in the experiment up to 40 GPa, and the calculations predict that the ambient-pressure structure remains stable in excess of 80 GPa (i.e., the system relaxes back to the Sm_2Co_{17} structure after small, symmetry-breaking displacements of the atoms). The experimental (calculated) unit-cell volumes have been fit by a third-order Birch-Murnaghan equation of state [Fig. 1(d)] to obtain a bulk modulus of 157 GPa (142 GPa) [34]; the error in the determination of the bulk modulus from these fits amounts to approximately 10%. The values of B' for the experimental and calculated fits are comparable, and the difference in the bulk moduli is within the errors due to the equation-of-state fits. The excellent agreement between theory and experiment for the structure under pressure suggests that our DFT model for Sm_2Co_{17} is a good starting point for examining calculated magnetic properties under pressure.

B. Electronic structure under pressure

The projected density of states (pDOS) for the Co and Sm valence band states in Sm_2Co_{17} at the equilibrium volume are presented as functions of binding energy ($E - E_F$) in Fig. 2. The Co majority spin (hereafter referred to as "spin up") $3d$ band is fully occupied and sits below the Fermi level, while
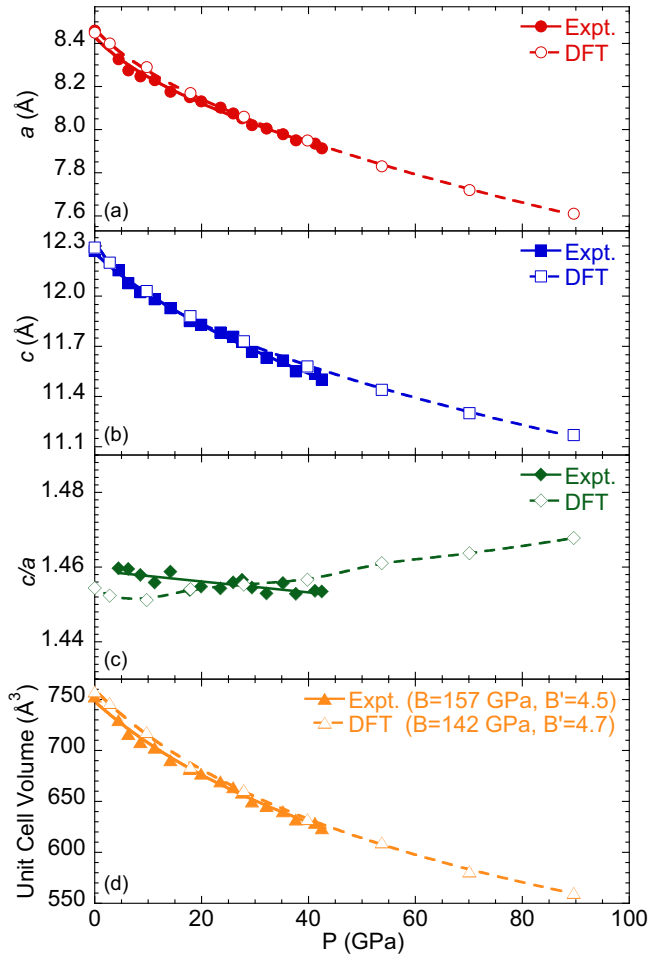
FIG. 1. (Color online) The experimental (closed symbols) and calculated (open symbols) crystal structure parameters of Sm_2Co_{17} under pressure: (a) basal plane a-axis lattice parameter, (b) c-axis lattice parameter, (c) c/a ratio, and (d) the unit-cell volume. Lines in (a)–(c) are guides to the eye, while those in (d) are fits to the third-order Birch-Murnaghan equation of state. Error bars returned from structural refinements are smaller than the experimental points.

the minority spin (hereafter referred to as "spin down") band is partially occupied. The calculated band positions and widths are comparable to that seen in elemental, hexagonally close-packed (hcp) Co [35,36]. The Co spin-down pDOS displays a sharp edge at a binding energy of about -0.65 eV. Below this energy, the spin-down pDOS dramatically increases.

Additionally, Fig. 2 displays the pDOS for the Sm $4f$ and $5d$ states. The spin-down $4f$ states reside about 5 eV below the Fermi level, but a small amount of f character is present near the Fermi level. Note that our calculations do not include spin-orbit coupling effects, thus the details of the $4f$-band splittings are not expected to be fully accurate; the unoccupied, spin-up Sm $4f$ states are calculated to be about 5 eV above the Fermi level. Nevertheless, the overall position of the occupied Sm $4f$ band is in reasonable agreement with ambient-pressure XPS measurements. Integration of the Sm $4f$ band up to the Fermi level yields a total of 5.2 electrons per Sm atom, suggesting a configuration very close to that of a Sm 3^+ ion. Consistent
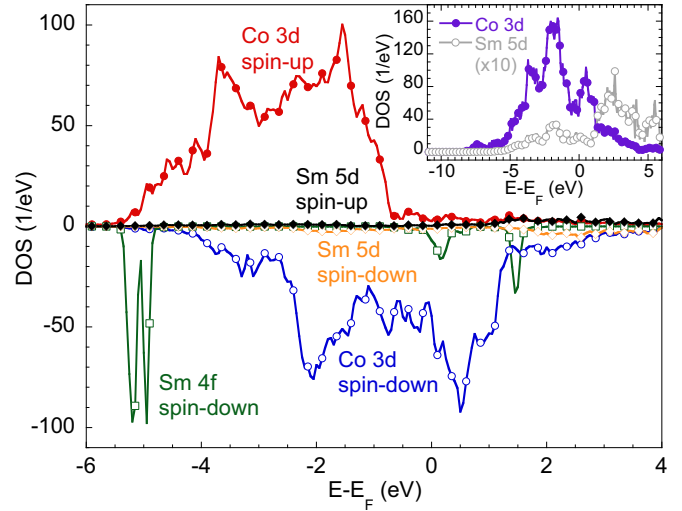

FIG. 2. (Color online) The ambient-pressure, spin-resolved, partial densities of states (DOS) from both Sm and Co states plotted versus binding energy $E - E_F$. The spin-up states are plotted on the positive, vertical axis, while the spin-down states are plotted along the negative, vertical axis. Inset: the spin-summed contribution from the Co $3d$ and Sm $5d$ states, suggesting Sm-Co hybridization.

with previously advanced explanations of the Sm-Co coupling [5,16,17], there appears to be significant hybridization between the Co $3d$ and Sm $5d$ states, as seen in the inset of Fig. 2 where the respective pDOS display very similar energy dependencies below E_F.

We find that the lowest-energy state corresponds to a state where the Co $3d$ and Sm $4f$ spin moments are oriented antiparallel to each other (i.e., the Sm $4f$ states are spin down). Note that there is some disagreement here in more recently published first-principles calculations that find the opposite situation, where both the Co $3d$ and Sm $4f$ spin moments are parallel [18,19]. Part of the difficulty here is the well-known sensitivity of the DFT+U method to the initial guess in the density matrix that enters into the DFT+U onsite correction term. Our finding of antiparallel spin moments and, thus, parallel total moments is consistent with long-standing explanations for the Sm-Co systems [5,16,17].

The ambient-pressure Co moment is calculated to be about 1.6 μ_B, nearly identical to that of hcp Co [37] and consistent with previous calculations for $SmCo_5$ [38]. The Sm moment is calculated to be about 5.7 μ_B. The lack of spin-orbit coupling in our calculations results in a practically quenched orbital angular momentum for the f states of the Sm^{3+} ion, yielding a spin-only moment in the absence of an exchange parameter equal to 5 μ_B, consistent with similar calculations by Richter as well as Liu and Altounian [18,39]. Although the Sm moment is dominated by the Sm $4f$ electrons, the $5d$ states also contribute a small spin polarization.

The total (Sm and Co electronic states) spin-up and spin-down DOS at 0, 28, and 54 GPa are shown in Fig. 3. With pressure, the $4f$ states of the Sm atoms move slightly deeper below the Fermi level, implying that the Sm moment should be only weakly affected by pressure [Fig. 6(a)]; its small reduction is likely a consequence of changes in the $5d$ contribution to the
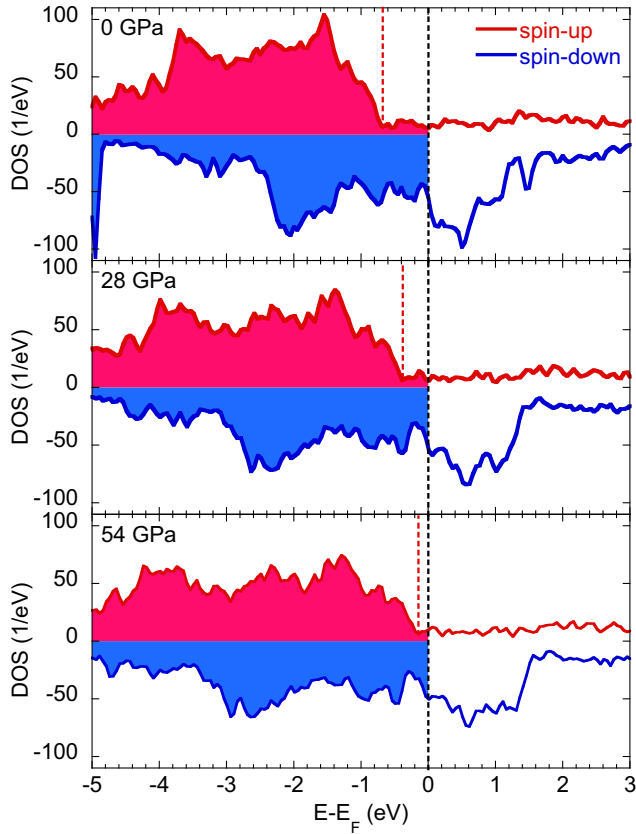
FIG. 3. (Color online) The computed, total density of states (DOS) decomposed into the spin-up (red line, positive axis) and spin-down (blue line, negative axis) spins for different calculated pressures as functions of energy E. The Fermi level (E_F) is marked with a vertical, black dashed line; shaded regions denote the occupied DOS. The sharp edge in the spin-up DOS, predominantly composed of Co $3d$ states, is demarcated by a red, dashed line.

moment rather than the $4f$ states. The predominant, pressure-induced changes in the band structure are driven by the Co $3d$ states. Under pressure, the spin-down bands shift slightly down, while the spin-up bands shifts up towards the Fermi level. The movement of the spin-up bands is best visualized by the shift in the spin-up edge, shown as a vertical, red, dashed line in Fig. 3. A similar feature is predicted in the band structure of YCo$_5$, and the pressure-induced crossing of this spin-up edge is implicated in driving a magnetoelastic volume collapse [40]. However, in Sm$_2$Co$_{17}$, the spin-up edge is predicted to remain below the Fermi level up to 54 GPa. Extrapolating the change in the theoretical position of the spin-up edge with pressure would imply a Fermi level crossing near 70 GPa. Thus, Sm$_2$Co$_{17}$ is not expected to be susceptible to magnetoelastic collapse until pressures well in excess of those achieved in our experiments. The shifts in the spin-up and -down bands result in a redistribution of the electron spin states, yielding a reduction in Co moment under pressure. However, because the spin-up edge remains below the Fermi level, the Co moment not only survives up to 54 GPa, but it remains substantial, decreasing by less than 10% for a nearly 20% compression [Fig. 6(b)].

C. Magnetic measurements under pressure

1. Local Sm moments

Experimental measurements of magnetism under pressure have been notoriously difficult to perform. While neutron scattering yields a direct coupling between the neutron spin and the moments of any system under investigation, these techniques typically do not lend themselves to the small sample volumes required for generating static high pressures. However, the latest-generation synchrotron x-ray sources have enabled pressure-dependent measurements of local and ordered magnetic moments through the techniques of nonresonant x-ray emission spectroscopy (XES) and x-ray magnetic circular dichroism (XMCD).

Nonresonant XES at the $K\beta$ emission line has been used as a probe of the magnetic moment in d-block transition-metal minerals and compounds under pressure [41–44]. In d-electron systems, the sensitivity of the XES signal to the Fe moment (spin dominated) is brought about by an overlap of the $2p$ and $3d$ orbitals. For rare-earth systems, the analogous emission line is the $L\gamma_1$ line, a $4d \rightarrow 2p$ transition. Although not as extensively studied as the $K\beta$ spectroscopies, the $L\gamma_1$ emission line is thought to have a similar sensitivity to the local rare-earth moment (or spin state) through a significant overlap between the $4d$ and $4f$ orbitals [45–47]. A schematic of the atomic process is shown in Fig. 4(d). An x-ray with an energy above the Sm L edge excites a $2p$ electron into the continuum, and the $2p$ core hole is filled by a decay from the $4d$ manifold; the emitted photon from this process is the $L\gamma_1$ emission line. The final-state $4d$ core hole of the $L\gamma_1$ emission process presumably interacts with the magnetic configuration of the $4f$ state (in analogy to the Fe $K\beta$ scenario), leading to an energy splitting between parallel and antiparallel spin states. This energy splitting manifests in the XES spectrum as a lower-energy satellite peak that resides about 20 eV below the main $L\gamma_1$ line. Representative XES spectra for Sm$_2$Co$_{17}$ at three different pressures are shown in Figs. 4(a)–4(c), where the main $L\gamma_1$ lines and the satellite peaks are clearly visible.

Although XES has found success in describing the evolution of moments under pressure [41–44], quantitative analysis of the results can still be complicated. Here, we adopt the technique of the integrated absolute difference (IAD) approach, which has been successfully employed with Fe-bearing systems to provide a quantitative analysis of changes in the spectra under pressure [48,49]. An IAD analysis of a spectrum begins with that spectrum being normalized such that its integral is unity. A reference spectrum (also unit normalized) is subtracted from the spectrum to yield a difference spectrum, and the absolute value of that difference spectrum, or the IAD, becomes the quantitative metric for changes in the magnetic configuration of the Sm $4f$ electrons. For the case of Sm$_2$Co$_{17}$ under pressure, we have used our low-pressure spectrum at 2.4 GPa as the reference spectrum. This reference spectrum along with the difference spectra derived from it are included in Figs. 4(a)–4(c).

The IAD for Sm$_2$Co$_{17}$ is shown as a function of pressure in Fig. 4(e), where the error bars represent uncertainty in the measurements due to noise. Using a low-pressure spectrum as the reference, as opposed to a fixed- or zero-moment reference, has two relevant consequences: (1) the magnitude of the
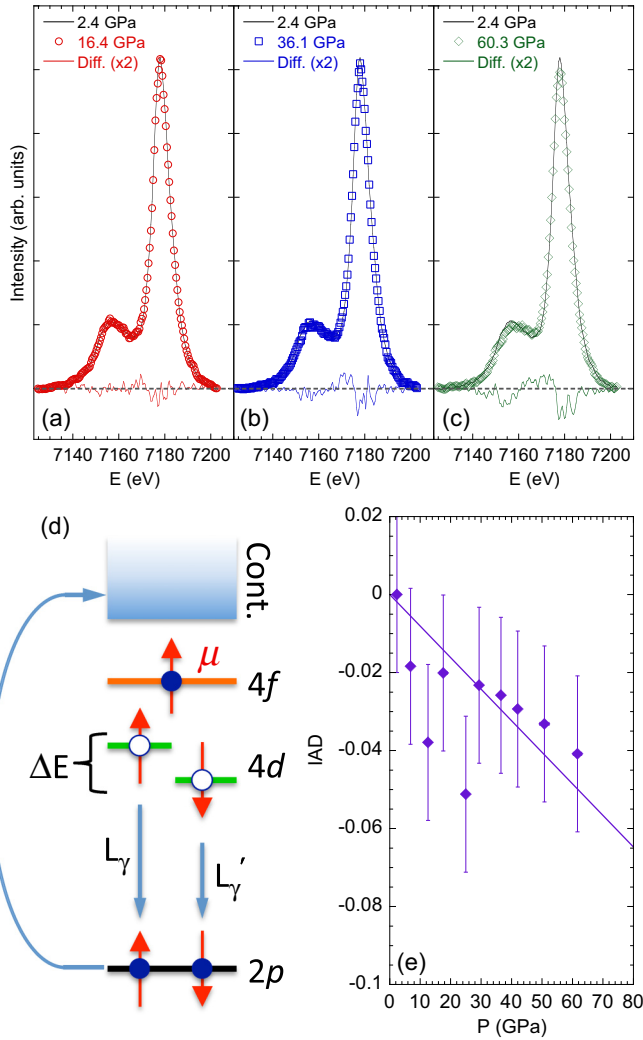
FIG. 4. (Color online) (a)–(c) Representative Sm $L\gamma_1$ x-ray emission spectra under pressure. The low-pressure (2.4 GPa) spectrum is plotted as a solid, black line in each panel, while the open symbols represent the spectra at 16.4, 36.1, and 60.3 GPa. The differences between the high- and low-pressure spectra are plotted as solid, colored lines. The dotted, horizontal black line is zero. (d) A schematic representation of the atomic XES process for the Sm $L\gamma_1$ line. A photon with an energy above the Sm L edge excites a $2p$ electron into the continuum, and that $2p$ core hole is filled by a decay from the $4d$ manifold. The spin of the final-state $4d$ core hole interacts with the magnetic configuration of the $4f$ shell, lifting the degeneracy of the $4f$ state and manifesting two transitions separated by ΔE. (e) The IAD (see text) as a function of pressure implies a decreasing Sm f moment under pressure; the solid line is a guide to the eye. Error bars are estimated from the noise in the XES signals.

IAD does not indicate whether the magnetic configuration is changing so as to reduce or increase the observed moment, and (2) the IAD becomes a relative, rather than absolute, measure. The problem of (1) can be averted by assessment of the magnitude of the $L\gamma_1$ satellite peak and its position as a function of pressure, whereas the problem of (2) can be addressed by having a fixed point (e.g., a zero-pressure measurements of the moment) as well as a calibration of
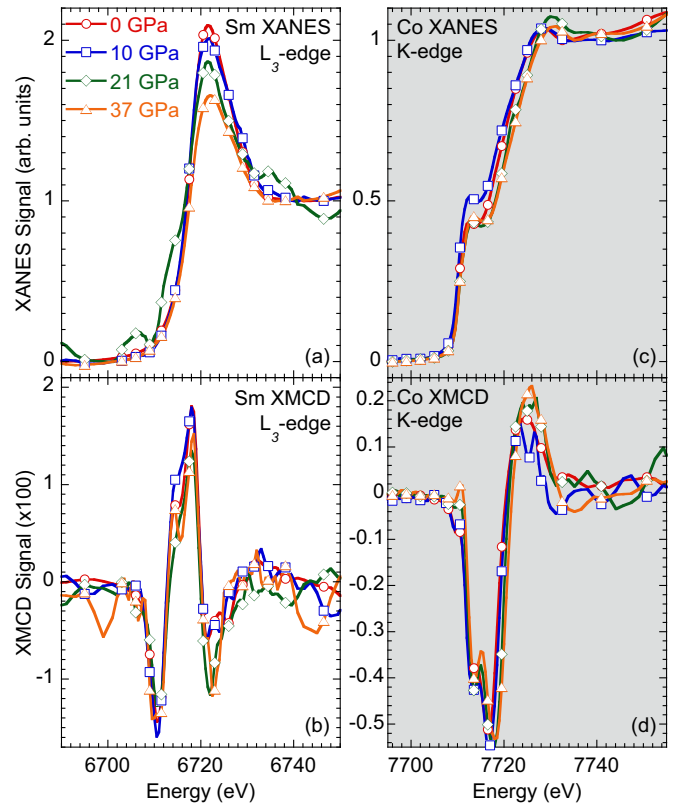

FIG. 5. (Color online) The Sm L_3-edge XANES (a) and XMCD (b) as well as the Co K-edge XANES (c) and XMCD (d) spectra as a function of incident photon energy for the four different pressures investigated.

the IAD magnitude to the local moment. Because the peak splitting between the main peak and the satellite ΔE in the light rare earths increases across the series [45], ΔE has been linked to the moment (or spin state) of the $4f$ electrons. The satellite peak at 60.3 GPa has a slightly lower ΔE than that at 2.4 GPa [Fig. 4(c)], suggesting that the moment or spin state of the Sm $4f$ electrons is decreasing with pressure. This behavior is qualitatively consistent with the decreasing Sm moment observed in theoretical calculations; however, while the IAD has been calibrated to the local moment in tetrahedrally coordinated Fe-based systems [49], no such calibration exists for Sm atoms in the hexagonal environment of the Sm_2Co_{17} structure. Thus, the experiments are consistent with the decreasing moment predicted from theory, but they cannot, at present, *quantitatively* confirm our theoretical predictions.

2. Ordered Sm and Co moments

Figure 5 shows the XANES and XMCD results for Sm_2Co_{17} under pressure at the Sm L_3 ($2p \rightarrow 5d$ transition) and Co K edges ($1s \rightarrow 4p$ transition). The XANES signal is plotted as the absorbance, that is, $\ln(I_0/I)$, where I_0 is the incident x-ray intensity and I is the measured intensity after the DAC. The spectra have been normalized such that the "jump" (i.e., the intensity after the edge) is equal to unity, and the XMCD signal, being a difference between XANES spectra with different

helicities, is subject to the same normalization factor. The Sm L_3-edge data inherently suffer from more noise than the Co K-edge measurements because the lower energy of the Sm L_3 edge is subject to more attenuation by the diamond anvils and the Sm content is significantly smaller than the Co content of Sm_2Co_{17}.

As is typical with Sm L_3-edge spectroscopy [Fig. 5(a)], the XANES spectra of Sm_2Co_{17} show a relatively large "white line," the peak just above the absorption edge, centered near 6722 eV. The position of the white line suggests that the Sm ions in Sm_2Co_{17} have a valence close to 3^+ [50]. With pressure, the intensity of the white line decreases. The pressure-induced reduction in the white-line intensity of lanthanide elements is understood to be a consequence of $6s$-$5d$ charge transfer that reduces the number of empty $5d$ states [51]. However, the white line does not shift to lower energy, indicating that the valence of the Sm ions remains very close to 3^+ over the measured pressure range.

The Co K-edge spectroscopy under pressure is shown in Figs. 5(c) and 5(d). Although the Sm L_1 edge is located at 7737 eV, the stoichiometry of the sample and the Sm L_1-edge cross section preclude the observation of the Sm signal in the Co K-edge XANES. As in elemental Co, there is a near-edge peak near 7712 eV (at ambient pressure) that corresponds to transitions into Co $3d$-$4p$ hybridized final states [52]. With pressure, this near-edge peak shifts to higher energy by about 1 eV by 37 GPa. Unlike elemental Co under pressure, where the $3d$-$4p$ near-edge peak gains intensity under pressure, the intensity of the near-edge peak in Sm_2Co_{17} shows no systematic tendency with pressure, varying between 0.5% and 1.5% of the jump. In elemental Co, the increase in intensity in the near-edge peak has been associated with Co $3d$-band broadening and an increased hybridization between the Co $3d$ and $4p$ states [52]. In contrast, the pressure dependence (or lack thereof) of the near-edge peak of Sm_2Co_{17} suggests that pressure does not drive additional Co $3d$-$4p$ hybridization.

Although the vast majority of the magnetism in Sm_2Co_{17} resides with the Sm $4f$ and Co $3d$ electrons, the large XMCD resonances of the Sm M and Co L edges, which directly couple to the "magnetic" electrons, are unavailable in a DAC because, at these soft x-ray energies (just below 1100 and 800 eV, respectively), the amount of diamond in a typical DAC is far too absorbing to permit measurements. Fortunately, a small polarization can be induced in the Sm $5d$ and Co $4p$ states, manifesting a dichroic signal, albeit much smaller than that of the soft x-ray edges, at the Sm L_3- and Co K edges. These edges occur in the hard x-ray regime, and are thus amenable to DAC measurements. These hard x-ray XMCD signals do not permit the application of the magneto-optical sum rules available in the the soft x-ray regime [53,54], meaning that the spin and orbital components of the magnetic moments cannot be disentangled, nor can the absolute moment of each element be easily quantified. Nonetheless, the rare-earth L_3- and transition-metal K-edge XMCD have been shown to be proportional to the total moment, providing a means of investigating the pressure dependence of the element-specific magnetic moments [55,56].

Like other rare-earth systems, the XMCD signal for Sm_2Co_{17} is substantial, with a maximum intensity near 2% of the jump [57]. The Co XMCD signal of Sm_2Co_{17} looks

nearly identical to that of pure Co [52]. In the absence of magneto-optical sum rules, *ab initio* calculations can in principle provide insight into the relative orientation of Sm $4f$ and Co $3d$ magnetic moments. An attempt was made to model the XMCD data with the FDMNES code [33]. While these simulations provided some evidence in support of FM coupling, limitations in the treatment of $4f$ electrons within the LSDA+U method implemented in this code yielded $4f$ bands too close to the Fermi level, and thus preventing a definitive conclusion regarding the relative orientation of the Sm and Co moments. The tendency for true FM coupling is consistent with previous work describing the $RETM_5$ and RE_2TM_{17} systems as having antiparallel spin coupling arising from either RKKY interactions between the conduction band and the localized, rare-earth $4f$ electrons or direct $5d$-$3d$ exchange between the rare-earth and transition-metal sublattices [5,16,17].

In Sm_2Co_{17}, pressure has little effect on either the Sm or Co XMCD signals, yielding a pressure dependence of the Co XMCD that is markedly weaker than pure Co [52]. By 35 GPa, the XMCD signal of pure Co has decreased by almost 35%, whereas the Co K-edge XMCD signal of Sm_2Co_{17} shows little to no change between ambient pressure and 37 GPa. The Sm XMCD signals shows no pressure-dependent change in sign, meaning that the ferromagnetic configuration is preserved under pressure. Furthermore, the pressure dependence of the Sm XMCD signal is weak, implying little dependence on structural parameters and highlighting the importance of direct exchange, as opposed to RKKY mechanisms, in controlling magnetism in Sm_2Co_{17} [58].

The absolute values of the Sm and Co XMCD signals have been integrated to obtain an integrated XMCD intensity. The integration ranges were 6700–6730 eV for Sm and 7700–7730 eV for Co. The integrated XMCD intensities have been normalized such that the ambient-pressure values are equal to the calculated moments at zero pressure. The error for the XMCD intensities under pressure have been estimated from integration of the absolute value of the high-energy side ($>$6730 eV for Sm, $>$7730 for Co) of the XMCD spectra, which is assumed to show zero dichroism. The variance of these integrals is used as the error.

The measured XMCD signals have been normalized to coincide with the theoretical predictions for the elemental Sm and Co moments at zero pressure. The normalized XMCD intensities as well as the calculated moments are included in Fig. 6 and plotted as functions of the atomic volume for each element. The Sm atomic volume (V_{Sm}) was assumed to be 26.5 Å at ambient pressure, and its compression has been calculated by scaling the ambient-pressure value with three times the change in the nearest-neighbor Sm-Co bond (l_{SC}) under pressure ($\Delta V_{Sm}/V_{Sm} = 3\Delta l_{SC}/l_{SC}$). The Co atomic volume has been calculated by subtracting the as-calculated Sm contribution to the unit-cell volume (six atoms per unit cell) from the measured unit-cell volumes and dividing the result by the remaining 51 Co atoms of the unit cell. The XMCD data as a function of compression (Co or Sm atomic volume) indicate that both the Sm and Co moments are extremely robust, and the data, within error, are in reasonably good agreement with our theoretical calculations. As a comparison, the Co moment of elemental, hcp Co is included in
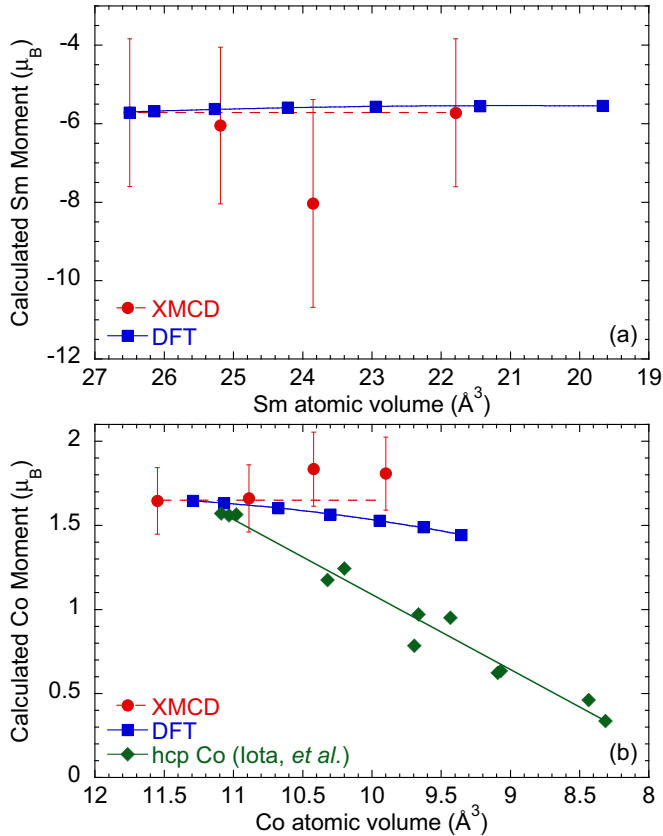
FIG. 6. (Color online) The theoretical and measured (normalized to theory at $P = 0$) Sm (a) and Co (b) moments as functions of elemental volume (see text). The evolution of the Co moment under pressure is included for comparison in (b). Error bars are estimated from the noise in the XMCD spectra far from the edge. The lowest compression (highest pressure) data point in each pane corresponds to 54 GPa.

FIG. 7. (Color online) Normalized magnetization determined from XMCD measurements for the Sm L_3 (left panel) and Co K edges (middle panel) plotted as functions of applied magnetic field. The hysteresis loops are offset vertically for clarity. Ambient-pressure magnetization of an aligned powder embedded in epoxy determined at 100 K using a SQUID magnetometer (right panel) and displaying a coercivity near 2 kOe.

IV. CONCLUSIONS

Sm_2Co_{17} displays robust ferromagnetism under pressure. The local Sm moment, as determined by XES measurements, shows little pressure-dependent evolution, and the ordered Sm and Co moments are similarly robust under compression. A ferromagnetic configuration is favored in our calculations, and the persistent XMCD signal of Sm_2Co_{17} implies that ferromagnetism persists even up to pressures near 40 GPa. Hysteresis measurements imply substantial coercivity even at high pressures, and also that the Sm and Co sublattices are strongly coupled, responding in lock-step to changes in field.

Fig. 6(b). From the measurements and theoretical calculations, it is clear that the Co moment of Sm_2Co_{17} under pressure is more robust than that of hcp Co, with Sm_2Co_{17} having a Co moment approximately twice as large as hcp Co for a given compression.

The XMCD technique also permits a measurement of the element-specific coercivity under pressure. In this case, the intensity at the largest XMCD signal (positive for Co, and negative for Sm) is recorded to yield a metric proportional to the moment as a function of applied field. These measurements are displayed in Fig. 7; an ambient-pressure, 100-K magnetization loop recorded with a SQUID magnetometer is included for comparison. The hysteresis loops have been normalized such that the value at maximum (minimum) field is 1 (-1), and the coercivity is determined by the half-width of the loop at zero normalized magnetization. Hysteresis measurements at the Sm L_3 edge at 21 and 37 GPa were not performed with sufficient signal-to-noise ratios. The coercivity decreases with pressure, but Sm_2Co_{17} remains a "hard ferromagnet" with a coercivity above 1 kOe up to 37 GPa. Where measured together, the Sm and Co elemental coercivities appear to be equivalent within error, suggesting that both sublattices respond in lock-step to changes in field.
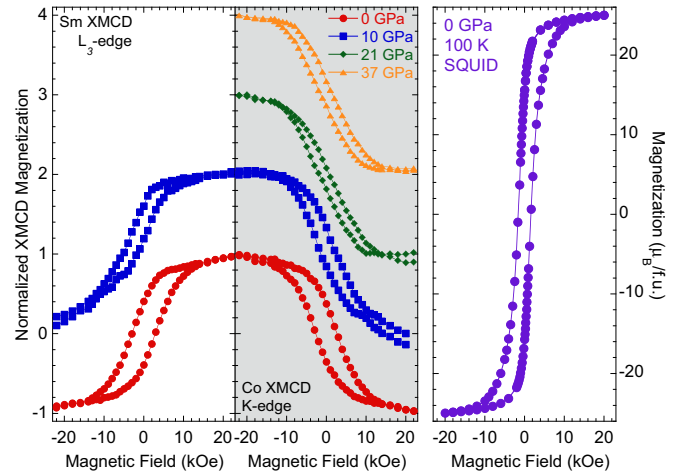
[1] K. H. J. Buschow, Rep. Prog. Phys. **54**, 1123 (1991).

[2] J. F. Herbst, Rev. Mod. Phys. **63**, 819 (1991).

[3] J. M. D. Coey, *Magnetism and Magnetic Materials* (Cambridge University Press, Cambridge, 2009).

[4] R. L. McCurrie, in *Ferromagnetic Materials*, edited by E. P. Wohlfarth (North-Holland, Amsterdam, 1982), Vol. 3, p. 107.

[5] K. Kumar, J. Appl. Phys. **63**, R13 (1988).

[6] J. Luo, J. K. Liang, Y. Q. Guo, Q. L. Liu, L. T. Yang, F. S. Liu, and G. H. Rao, Appl. Phys. Lett. **84**, 3094 (2004).

[7] R. F. Sabirianov, A. Kashyap, R. Skomski, S. S. Jaswal, and D. J. Sellmyer, Appl. Phys. Lett. **85**, 2286 (2004).

[8] J. Sayama, K. Mizutani, T. Asahi, and T. Osaka, Appl. Phys. Lett. **85**, 5640 (2004).

[9] J. Sort, S. Suriñach, J. S. Muñoz, M. D. Baró, J. Nogués, G. Chouteau, V. Skumryev, and G. C. Hadjipanayis, Phys. Rev. B **65**, 174420 (2002).

[10] H. Kronmüller and D. Goll, Phys. B (Amsterdam) **319**, 122 (2002).

[11] Y. Wang, Y. Li, C. Rong, and J. P. Liu, Nanotechnology **18**, 465701 (2007).

[12] B. Z. Cui, W. F. Li, and G. C. Hadjipanayis, Acta Mater. **59**, 563 (2011).

[13] K. H. J. Buschow and A. S. van der Groot, J. Less-Common Met. **14**, 323 (1968).

[14] A. S. Ermolenko, IEEE Trans. Magn. **MAG-12**, 992 (1976).

[15] J. M. D. Coey, IEEE Trans. Magn. **47**, 4671 (2011).

[16] I. A. Campbell, J. Phys. F: Met. Phys. **2**, L47 (1972).

[17] M. S. S. Brooks, T. Gasche, S. Auluck, L. Nordström, L. Severin, J. Trygg, and B. Johansson, J. Appl. Phys. **70**, 5972 (1991).

[18] X. B. Liu and Z. Altounian, Comput. Mater. Sci. **50**, 841 (2011).

[19] P. Larson, I. I. Mazin, and D. A. Papaconstantopoulos, Phys. Rev. B **69**, 134408 (2004).

[20] A. Hammersley, S. Svensson, M. Hanfland, A. Fitch, and D. Häusermann, High Press. Res. **14**, 235 (1996).

[21] J. P. Perdew, K. Burke, and M. Ernzerhof, Phys. Rev. Lett. **77**, 3865 (1996).

[22] M. Methfessel and A. T. Paxton, Phys. Rev. B **40**, 3616 (1989).

[23] P. Giannozzi, S. Baroni, N. Bonini, M. Calandra, R. Car, C. Cavazzoni, D. Ceresoli, G. L. Chiarotti, M. Cococcioni, I. Dabo, A. Dal Corso, S. Fabris, G. Fratesi, S. de Gironcoli, R. Gebauer, U. Gerstmann, C. Gougoussis, A. Kokalj, M. Lazzeri, L. Martin-Samos, N. Marzari, F. Mauri, R. Mazzarello, S. Paolini, A. Pasquarello, L. Paulatto, C. Sbraccia, S. Scandolo, G. Sclauzero, A. P. Seitsonen, A. Smogunov, P. Umari, and R. M. Wentzcovitch, J. Phys.: Condens. Matter **21**, 395502 (2009).

[24] D. Vanderbilt, Phys. Rev. B **41**, 7892 (1990).

[25] E. G. Moroni, G. Kresse, J. Hafner, and J. Furthmüller, Phys. Rev. B **56**, 15629 (1997).

[26] A. M. Rappe, K. M. Rabe, E. Kaxiras, and J. D. Joannopoulos, Phys. Rev. B **41**, 1227 (1990).

[27] S. G. Louie, S. Froyen, and M. L. Cohen, Phys. Rev. B **26**, 1738 (1982).

[28] M. Cococcioni and S. de Gironcoli, Phys. Rev. B **71**, 035105 (2005).

[29] C. Clavaguéra-Sarrio, V. Vallet, D. Maynau, and C. J. Marsden, J. Chem. Phys. **121**, 5312 (2004).

[30] V. Vallet, P. Macak, U. Wahlgren, and I. Grenthe, Theor. Chem. Acc. **115**, 145 (2006).

[31] G. La Macchia, I. Infante, J. Raab, J. K. Gibson, and L. Gagliardi, Phys. Chem. Chem. Phys. **10**, 7278 (2008).

[32] X.-D. Wen, R. L. Martin, L. E. Roy, G. E. Scuseria, S. P. Rudin, E. R. Batista, T. M. McCleskey, B. L. Scott, E. Bauer, J. J. Joyce, and T. Durakiewicz, J. Chem. Phys. **137**, 154707 (2012).

[33] Y. Joly, Phys. Rev. B **63**, 125120 (2001).

[34] F. Birch, Phys. Rev. **71**, 809 (1947).

[35] R. A. Ballinger and C. A. W. Marshall, J. Phys. F: Met. Phys. **3**, 735 (1973).

[36] J. S. Nelson, C. Y. Fong, and C. M. Perlov, J. Appl. Phys. **63**, 3046 (1988).

[37] N. Spaldin, *Magnetic Materials Fundamentals and Applications* (Cambridge University Press, Cambridge, 2011).

[38] Zhao Tie-Song, Jin Han-min, Guo Guang-hua, Han Xiu-feng, and Chen Hong, Phys. Rev. B **43**, 8593 (1991).

[39] M. Richter, J. Phys. D: Appl. Phys. **31**, 1017 (1998).

[40] H. Rosner, D. Koudela, U. Schwarz, A. Handstein, M. Hanfland, I. Opahle, K. Koepernik, M. D. Kuz'min, K.-H. Müller, J. A. Mydosh, and M. Richter, Nat. Phys. **2**, 469 (2006).

[41] S. Speziale, A. Milner, V. E. Lee, S. M. Clark, M. P. Pasternak, and R. Jeanloz, Proc. Natl. Acad. Sci. USA **102**, 17918 (2005).

[42] J.-F. Lin, V. V. Struzhkin, S. D. Jacobsen, M. Y. Hu, P. Chow, J. Kung, H. Liu, H.-K. Mao, and R. J. Hemley, Nature (London) **436**, 377 (2005).

[43] J.-P. Rueff and A. Shukla, Rev. Mod. Phys. **82**, 847 (2010).

[44] R. S. Kumar, Y. Zhang, Y. Xiao, J. Baker, A. Cornelius, S. Veermalai, P. Chow, C. Chen, and Y. Zhao, Appl. Phys. Lett. **99**, 061913 (2011).

[45] K. Jouda, S. Tanaka, and O. Aita, J. Phys.: Condens. Matter **9**, 10789 (1997).

[46] B. R. Maddox, A. Lazicki, C. S. Yoo, V. Iota, M. Chen, A. K. McMahan, M. Y. Hu, P. Chow, R. T. Scalettar, and W. E. Pickett, Phys. Rev. Lett. **96**, 215701 (2006).

[47] M. J. Lipp, A. P. Sorini, J. Bradley, B. Maddox, K. T. Moore, H. Cynn, T. P. Devereaux, Y. Xiao, P. Chow, and W. J. Evans, Phys. Rev. Lett. **109**, 195705 (2012).

[48] G. Vankó, T. Neisius, G. Molnár, F. Renz, S. Kárpáti, A. Shukla, and F. M. de Groot, J. Phys. Chem. B **110**, 11647 (2006).

[49] H. Gretarsson, A. Lupascu, J. Kim, D. Casa, T. Gog, W. Wu, S. R. Julian, Z. J. Xu, J. S. Wen, G. D. Gu, R. H. Yuan, Z. G. Chen, N.-L. Wang, S. Khim, K. H. Kim, M. Ishikado, I. Jarrige, S. Shamoto, J.-H. Chu, I. R. Fisher, and Y.-J. Kim, Phys. Rev. B **84**, 100509(R) (2011).

[50] I. Jarrige, H. Yamaoka, J.-P. Rueff, J.-F. Lin, M. Taguchi, N. Hiraoka, H. Ishii, K. D. Tsuei, K. Imura, T. Matsumura, A. Ochiai, H. S. Suzuki, and A. Kotani, Phys. Rev. B **87**, 115107 (2013).

[51] J. C. Duthie and D. G. Pettifor, Phys. Rev. Lett. **38**, 564 (1977).

[52] V. Iota, J.-H. P. Klepeis, C. S. Yoo, J. Lang, D. Haskel, and G. Srajer, Appl. Phys. Lett. **90**, 042505 (2007).

[53] B. T. Thole, P. Carra, F. Sette, and G. van der Laan, Phys. Rev. Lett. **68**, 1943 (1992).

[54] P. Carra, B. T. Thole, M. Altarelli, and X. Wang, Phys. Rev. Lett. **70**, 694 (1993).

[55] O. Mathon, F. Baudelet, J. P. Itié, A. Polian, M. d'Astuto, J. C. Chervin, and S. Pascarelli, Phys. Rev. Lett. **93**, 255503 (2004).

[56] F. Baudelet, S. Pascarelli, O. Mathon, J. P. Itié, A. Polian, M. D'Astuto, and J. C. Chervin, J. Phys.: Condens. Matter **17**, S957 (2005).

[57] D. Haskel, Y. C. Tseng, N. M. Souza-Neto, J. C. Lang, S. Sinogeiken, Ya. Mudryk, K. A. Gschneidner Jr., and V. K. Pecharsky, High. Press. Res. **28**, 185 (2008).

[58] K. H. J. Buschow, in *Ferromagnetic Materials*, edited by E. P. Wohlfarth (North-Holland, Amsterdam, 1980), Vol. 1, p. 297.